An Approach to Rockfall Hazard Scenarios Based on Earthquake Ground Motion

Antonella Peresan, Massimiliano Alvioli, Elisa Zuccolo, Franco Vaccari, and Hazem Badreldin

Abstract

After an earthquake event, major ground effects include landslides. In Italy, the most common type of earthquake-induced landslides are rockfalls. The assessment of the extent and magnitude of an earthquake-induced landslide event may be of importance for both preparedness and response operations. An earlier work devised a modeling chain including an empirical ground shaking scenario and a three-dimensional model for rockfalls, which can be calibrated and possibly applied in real time after an earthquake event. In this study, we explore the combined use of two physics-based methods for both earthquake and rockfall modeling and their possible contribution towards a better understanding of the triggering mechanisms and characterization of seismically induced rockfalls. Specifically, by modeling a set of ground shaking scenarios, which account for increasingly complex details (including multiple seismic events, as well as point and extended sources) and the related rockfall scenarios, we aim to capture the main spatial patterns of observed rockfalls. Application of the proposed modeling chain suggests an advantage of using multiple sources over a single source, and point sources with respect to approximate extended representations when constrained by limited available data. This follows from the comparison of rockfall trajectory simulations for the Friuli 1976 event in Northern Italy with observed rockfalls induced by the seismic sequence. The obtained results evidence the opportunity of including topographic effects in the ground shaking simulations and highlights the possibility of further investigating the cumulative effect of complex seismic sequences and their influence on modulating landslide susceptibility.

Keywords

Earthquake scenario modeling · Coseismic rockfalls · Seismic ground shaking · Physics-based models · Multi-hazard

1 Introduction

The response of slopes under the action of ground shaking caused by a strong earthquake, can result in ground deformations and failures. Major ground effects include landslides; in Italy, the most common type of earthquake-induced landslides are rockfalls. Numerous studies have demonstrated a strong connection between the spatial distribution pattern of coseismic landslides/rockfalls and ground motion intensities (e.g., Keefer 2000; Luzi and Pergalani 2000; Jibson 2011; Tiwari et al. 2017; Alvioli et al. 2024). Specifically speaking, for the 1997 Mw5.5 Umbria-Marche earthquake in Italy, the landslide density map was quite well correlated with Arias Intensity by Luzi and Pergalani (2000). These studies collectively emphasize the significant contributions of controlling factors in the occurrence and distribution of coseismic landslides. In a previous work (Alvioli et al. 2024), they sug-

A. Peresan (✉) · E. Zuccolo
Seismological Research Center, National Institute of Oceanography and Applied Geophysics - OGS, Udine, Italy
e-mail: aperesan@ogs.it; ezuccolo@ogs.it

M. Alvioli
Istituto di Ricerca per la Protezione Idrogeologica, Consiglio Nazionale delle Ricerche, Perugia, Italy
e-mail: massimiliano.alvioli@irpi.cnr.it

F. Vaccari
Department of Mathematics, Informatics and Geosciences, Trieste, Italy
e-mail: vaccari@units.it

H. Badreldin
Seismological Research Center, National Institute of Oceanography and Applied Geophysics - OGS, Udine, Italy

National Research Institute of Astronomy and Geophysics, Cairo, Egypt
e-mail: hbadreldin@ogs.it

B. Abolmasov et al. (eds.), *Progress in Landslide Research and Technology, Volume 3 Issue 2, 2024*, Progress in Landslide Research and Technology, https://doi.org/10.1007/978-3-031-72736-8_8

gested a method for rapid post-earthquake rockfall scenario assessment, adopting ground-shaking estimates from empirical models (i.e. Ground Motion Models, GMMs) and the three-dimensional model STONE for rockfall trajectories. In the proposed method, ground-shaking maps corresponding to the May sixth 1976 Friuli earthquake (FVG, Friuli Venezia Giulia region, North-Eastern Italy) were used to suppress the probability of activation of rockfall sources at locations with low ground shaking, while enhancing that in areas close to the epicenter. Results of the modeling chain compared with an accurate inventory of earthquake-induced rockfalls (Govi 1977), suggested that the framework may be suitable for rapid rockfall impact assessment using ground-shaking estimates, in the immediate aftermath of a seismic event (Tanyaş et al. 2019). Here, we explore the possibility of replacing the adopted GMM with the physical modeling of seismic waves propagation, seeking an improvement of the agreement between the full modeling chain results and the rockfalls observed after the FVG 1976 earthquake sequence (see also Valagussa et al. 2014).

The study area (Fig. 1) is prone to a high seismic hazard, as confirmed by historical seismicity (Rovida et al. 2022) and studies based on morphostructural analysis (Gorshkov et al. 2009). The region is on the Alps-Dinarides junction, with compressional seismotectonic regime, with E-W trending thrust systems, mostly south dipping, with a subordinate strike-slip component to the east. Seismicity, spatial, and kinematic characteristics of main seismogenic sources of the area are summarized in Slejko et al. (1999), Bressan et al. (2018), and Aoudia et al. (2000). Complex seismic sequences are possible in this region (Peresan and Gentili 2018), the most damaging and recent one being the sequence associated with the 1976 FVG earthquake. Accordingly, this study aims at assessing the possible combined use of physics-based methods for both earthquake and rockfall modeling, towards an improved characterization of seismically induced rockfalls.

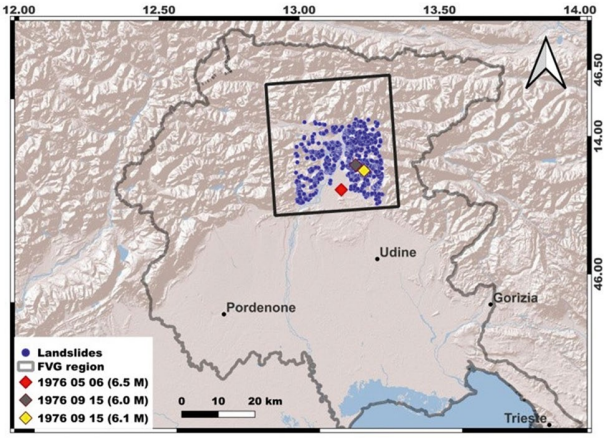

Fig. 1 Location of the study area within the FVG region (delimited in brown), illustrating the ground motion simulation domain (black rectangle). The map includes the earthquake epicentres of the Mw = 6.5 sixth May 1976 main shock (red diamond), and its strongest aftershocks (grey and yellow diamonds for the first and second aftershock, respectively). The rockfalls location points (blue circles) are from Govi inventory (1977)

Specifically, by modeling a suite of ground shaking scenarios, which capture increasingly complex features of earthquakes occurrence (including multiple seismic events, point and extended source representations), we attempt to investigate the cumulative effect of a complex seismic sequence and its possible influence on modulating landslide susceptibility.

In the previous study (Alvioli et al. 2024) they used Peak Ground Acceleration (PGA) to represent ground shaking associated to the May sixth, 1976 mainshock. We obtained a PGA map with the ShakeMap software (Worden et al. 2020), using few ground motion observations available and the ground motion model (GMM) of Akkar and Bommer (2007). Despite being a fast tool for studying the dependence between rockfall occurrences and seismic shaking, shakemaps can be unreliable if based on limited data. In scenarios like the Friuli 1976 seismic sequence, the selected GMM plays a crucial role, highlighting their inherent limitations. In fact, the ergodic assumption required by GMMs is not always fulfilled in seismic scenarios. Moreover, GMMs may contain significant uncertainties and biases due to the limited data used to constrain them. Consequently, GMMs may not capture significant features of earthquake waveforms, such as topographic amplification, shaking duration, and rupture directivity. These characteristics are crucial in understanding phenomena like landslide occurrence (Fan et al. 2019; Dahal et al. 2023).

A better way for accurately estimating ground shaking intensity parameters involves the computation of broadband synthetic seismograms. This approach utilizes physics-based simulations that convolve the contributions of seismic source, and path to the site(s) of interest. Various methods exist to obtain synthetic seismograms (e.g., Panza et al. 2001, 2012; Igel 2016), each offering different levels of accuracy depending on the availability of parameters describing the seismic source (i.e. fault geometry and slip distribution) and subsurface mechanical properties along the propagation path. The calculation of synthetic seismograms requires geological/geophysical and seismological data from the region of interest, ensuring a comprehensive representation of seismic activity specific to that area. However, modeling a specific past event often involves considerable uncertainties, particularly when limited data is available to provide a basis for comparison with full waveform modeling. In the case of the FVG 1976 seismic sequence, significant uncertainty exists not only regarding the source process, but also concerning the epicenter's location (e.g, Aoudia et al. 2000, Rovida et al. 2022).

The main objective of this work is to answer the question: how well do the modeled ground shaking scenarios capture the spatial distribution of observed coseismic rockfalls, and which scenario(s) best fits such distribution? We conducted tests to explore the connection between ground motion acceleration and rockfall distribution patterns. We assessed if PGA maps from physics-based simulations using point and extended source models for the main shock alone can explain landslide distribution. Understanding this connection is crucial for gaining insights in pre-disaster prevention and implementing efficient mitigation strategies.

2 Methods

2.1 Physics-Based Ground Motion Simulations

Simulations of the FVG 1976 seismic sequence, including wave propagation from the source to the area of interest, allowed us to obtain synthetic seismograms in the $0 \leq f \leq 10$ Hz frequency band. Convolution of the source term with the Green function, according to the representation theorem, is a common way to do that. We modeled earthquake scenarios considering both point and extended source models approximation. In the calculation of Green's functions we represented the structural model by a semi-infinite space in plane and parallel inelastic layers, corresponding to laterally homogeneous media, using the discrete wavenumber technique-DWN (Pavlov 2009), which allows the computation of synthetic accelerograms also in the near field.

In the point-source case, we produced the synthetic accelerograms for double-couple point sources, which are scaled for their dimensions using the spectral scaling laws proposed by Gusev (1983), as reported in Aki (1987). This was accomplished by leveraging some modules of the Neo-Deterministic Seismic Hazard Assessment (hereafter referred to as NDSHA, Panza et al., 2001, 2012) package, which relies on defining earthquake ground motion through the calculation of synthetic seismograms for a range of earthquake scenarios. In the extended-source case, the fault surface is represented by a rectangle modeled as a grid of point sub-sources, whose seismic moment is calculated by considering each of them as a component of a realization of a non-stationary random process.

Assuming a realistic kinematic description of the rupture process, the extended seismic source model allows for generating a spectrum (in amplitude and phase) of the temporal function of the source that takes into account both the rupture process and the effects of directivity. We used the algorithm PULSYN06 (Gusev 2011) for the simulation of the space and time evolution of the rupture. For each scenario, different possible realizations of the rupture process can be considered to take into account the stochastic nature of the fault rupture. Each realization is characterized by a different slip distribution on the fault plane, nucleation point, and time evolution. However, in this study, only one realization for each considered seismic source was selected, thus neglecting the uncertainties associated with the rupture process.

From the set of complete synthetic seismograms, various maps of ground shaking describing the maximum ground shaking parameters at the bedrock can be extracted. From the several parameters representative of earthquake ground motion we have focused on the horizontal PGA (i.e., the vector sum of the two horizontal components) computed considering bedrock conditions.

2.2 Three-Dimensional Rockfall Modeling

We adopted the three-dimensional program STONE to simulate block trajectories initiated from user-defined grid cells (Guzzetti et al. 2002). In this work, and following previous work, we adopted a set of "static" rockfall sources singled out on a 10 m × 10 m digital topography with statistical considerations, specific of the area, based on a set of expert-mapped rockfall sources (Alvioli et al. 2021) within a large sample of slope units (Alvioli et al. 2020). Combination with seismic shaking allows selecting a subset of "static" rockfall sources, thus obtaining "dynamic" sources, specific of a particular earthquake. Running STONE with "dynamic" sources provides a probabilistic estimate of potential rockfalls triggered by the earthquake. Results by Alvioli et al. (2024) show that the data available for the FVG 1976 earthquake allows tuning of the parameters involved by the models in the framework outlined above. The same method, with few variations, was applied before either at smaller scale (Alvioli et al. 2022), and at national scale, using maps of maximum expected PGA with different return times (Alvioli et al. 2023).

2.3 Input Data and Results

To analyze the results of the modeling chain for seismically induced rockfalls adopted here, first applied in the same area by Alvioli et al. (2024), we show the main input data and outcome of different steps, leading to the final rockfall simulation maps. First, we show results for the PGA maps, obtained using different modeling approximations to describe the FVG 1976 seismic sequence sources, relating them to the real coseismic rockfall distribution triggered by the seismic sequence. Next, we analyze the different ground motion scenarios considering the landslides/rockfalls observed after the sequence. Finally, we show results of probabilistic simulations of rockfall trajectories by STONE

Table 1 Parameters of the seismic point sources considered in this study. The DISS-ID column also identifies the individual sources of the DISS 3.3.0 database (DISS Working Group 2021) used to retrieve the fault geometry for the extended source approximation. SRC stands for source; time in 24 h notation

No. SRC	Date	Time	Mw CPTI15	Lon. [deg]	Lat. [deg]	Depth [km]	Strike [deg]	Dip [deg]	Rake [deg]	DISS-ID	Mw DISS3.3.1
1	05/06/1976	20:00	6.45	46.24	13.12	5.7	290	30	105	ITIS120	6.5
2	09/15/1976	03:15	5.93	46.28	13.20	6.8	274	35	90	ITIS121	6.0
3	09/15/1976	09:21	5.95	46.30	13.17	11.2	276	35	110	ITIS122	6.1

model, with different ground motion scenarios and two parametrizations of the coupling between maps of PGA and rockfall sources.

We considered three earthquake sources of the FVG 1976 seismic sequence (Fig. 1), with a magnitude close to 6.0 or larger, for the physics-based simulations described in previous section. Table 1 lists the input parameters for the point source approximation (longitude, latitude, and depth), retrieved from the CPTI15 catalog (Rovida et al. 2022), to which the focal mechanisms taken from the Database of Individual Seismogenic Sources (DISS 3.3.0, DISS Working Group 2021) were associated. The DISS3.3.0 was also adopted as a reference database for the magnitude and fault geometry associated with the extended source models (Table 1).

The 1D structural models adopted for the computation of the Green's functions were defined according to the average models associated with the regional polygons previously defined in the framework of GNDT (*Gruppo Nazionale per la Difesa dai Terremoti* of the *Consiglio Nazionale delle Ricerche*, Rome) activities, which were widely adopted for NDSHA purposes (Panza et al. 2001, 2012). Each layer of the 1D structural model has homogeneous values of thickness, P-wave velocity, S-wave velocity, density, and quality factors associated with both P- and S- waves.

2.4 Ground Motion Modeling

The PGA values were estimated at regular grid points with a spacing 2 × 2 km, considering four different earthquake scenarios, namely: one earthquake point source (the main shock), three aggregated earthquake point sources, one earthquake extended source (the main shock) and three aggregated earthquake extended sources. The grid covering the study area is composed by 306 cells, for a total area of 1224 km^2 (Fig. 2). Subsequently, we compared the spatial distribution patterns of landslides/rockfalls and PGAs for the site of interest using the Quantum Geographic Information System (QGIS) tool.

Govi (1977) mapped the landslides collectively triggered by the earthquakes of May 6, 1976 (6.5 Mw), September 15, 1976 (6.0 Mw), and September 15, 1976 (6.1 Mw) altogether, and developed a landslide inventory consisting of 1007 landslide occurrences (Figs. 1 and 2). Moreover, to perform geo-statistical analyses and relate the landslides distribution with PGA values, the PGA computed at the centre of each grid cell is assigned to the entire grid cell; the resulting discrete spatial distribution of PGA accounts for actual density of modelling results and avoids interpolations. On account of seismic ground motion uncertainty and significance (particularly relevant considering that historical information largely relies on macroseismic data), it is important to note that a doubling of the values of shaking roughly corresponds to a variation of one degree in the scale of macroseismic intensities, as formally defined by Cancani (1904) and demonstrated, on solid numerical basis by Panza et al. (1997). Accordingly, six PGA thresholds are used, namely: 20–40; 40–80; 80–150; 150–300; 300–600; and > 600 gal, which roughly correspond to different macroseismic intensity levels of the Mercalli-Cancani-Sieberg Intensity scale (MCS).

In the case the main earthquake (i.e. Mw 6.5 6th May, 1976 earthquake) is modeled as a point source, for the ground shaking threshold PGA ≥ 40 gal an area equal to the 78% of the entire grid is identified, and all of the triggered landslides are located within this area, as shown in Fig. 2a and summarized in Table 2. When selecting the territory affected by the strongest shaking, namely for PGA ≥ 300 gal, we find that only 17% of the area is assigned this PGA value and about 70% of the observed landslides is missed (i.e. 70% of landslides are located outside the area where PGA ≥ 300 gal). While considering three earthquakes (i.e. 6th May, 1976, Mw 6.0 15th September, 1976, and Mw 6.1 15th September, 1976), simulated using the point source approximation, for the same PGA thresholds (i.e. PGA ≥ 40 gal and PGA ≥ 300 gal), 83% and 18% of the grid area is selected and none and 70% landslides are missed, respectively (Fig. 2b and Table 2). On the other hand, the extended source models (Fig. 2c, d) provide slightly different spatial patterns of ground motion and higher values of shaking, for both the May 6, 1976 earthquake scenario and for the three earthquake scenarios computed using point source model (Fig. 2a, b, respectively). When he extended source models are used, practically all the territory (99%) is selected and no landslides are missed in the case of PGA ≥ 40 gal, while for PGA ≥ 300 gal about 34% of the territory is

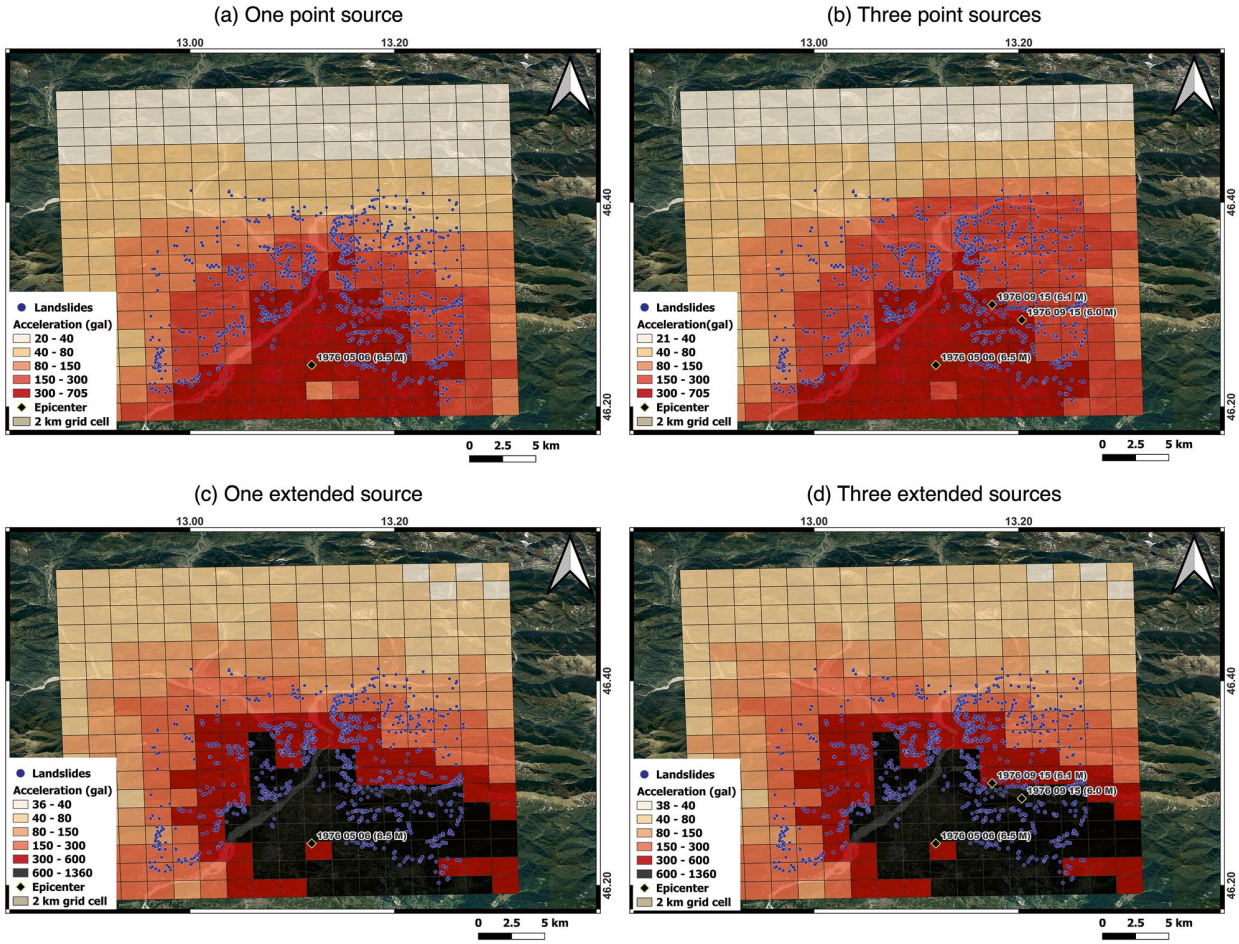

Fig. 2 Spatial distribution of modeled ground shaking (PGA [gal]) for: (**a**) the point-source main shock, (**b**) the three aggregated point sources, (**c**) the extended-source main shock and (**d**) the three aggregated extended sources. The locations of landslide points from Govi (1977) inventory are marked by blue dots. The grid cells are colored according to the PGA values computed at their central points. The black diamonds indicate the epicenters of the earthquakes considered in each panel

Table 2 Forecasting scores for the predictive analysis of rockfalls versus modeled ground shaking. The events to be predicted correspond to the landslide points reported in the inventory by Govi (1977). The errors obtained for each PGA threshold are compared for the four different models. The best prediction result, providing the lowest total error, is highlighted in bold

	One point source			Three point sources			One extended source			Three extended sources		
PGA threshold gal)	Area (α%)	Missed landslides (η%)	Total error (α + η)	Area (α%)	Missed landslides (η%)	Total error (α + η)	Area (α%)	Missed landslides (η %)	Total error (α + η)	Area (α%)	Missed landslides (η %)	Total error (α + η)
40	78.1	0.0	78.1	83.0	0.0	83.0	98.4	0.0	98.4	99.0	0.0	99.0
80	53.3	6.6	59.8	60.8	0.6	61.4	70.9	0.1	71.0	71.2	0.1	71.3
150	34.6	27.3	62.0	44.8	8.3	**53.1**	52.9	6.6	59.5	52.9	6.6	59.5
300	17.3	70.7	88.0	18.0	69.9	87.9	34.6	27.2	61.9	34.6	27.2	61.9
600	=	=	=	=	=	=	19.6	61.7	81.3	19.6	61.7	81.3

selected and about 27% landslides are missed (Table 2). The main information we obtained from the set of the four different simulations, shown in Fig. 2, is that using three earthquake sources either modeled according to a point or extended source approximation is important to reproduce the spatial distribution pattern of ground shaking that corresponds to, or encompass, the whole region affected by landslides.

2.5 Assessing the Correspondence Between Ground Motion and Rockfall Spatial Patterns

To explore the relation between the spatial pattern of ground motion and its possible effects on rockfall occurrences, we adopt a binary "forecasting" approach. Basically, we assess the presence (or absence) of rockfalls within a territory selected according to a specific value of the ground shaking parameter, and then we check whether the number of rockfalls identified based on ground motion is larger than that from a random guess. According to this scheme, by setting a threshold for a ground motion parameter, we identify the area (namely a set of grid cells) where this threshold is exceeded and which is assumed prone to the occurrence of rockfalls/landslides. When a landslide occurs within such *alerted area*, then it is counted as a *successful prediction*, otherwise it is referred as *failure to predict*; if no landslide occurs within a selected cell, then the cell is considered as a *false alarm*.

Following Molchan (1990), the results of this forecasting scheme can be characterized by two types of errors. The first one is the percentage η of failures to predict: $\eta = F/N$, where F is the number of failures to predict (i.e. rockfalls outside the alerted area) and N is the total number of occurred rockfalls. The second one is the percentage α of alarms: $\alpha = A/T$, where A is the extent of the alarmed area (the alerted cells) and T is the extent of the study area (the entire grid). The strength of a prediction is estimated by the analysis of the error diagram, collecting information on both types of errors. In order to characterize the quality of forecasting results in terms of the errors η and α, it is possible to consider any convex function $\Omega = f(\eta,\alpha)$; amongst the several possible functions, the sum of errors is the most straightforward and widely used for the evaluation of forecasting results (Molchan 1990, 1997).

Hence in this study the quality of rockfall predictions is quantified by the sum of errors: $\Omega = \eta + \alpha$, but different possible measures are possible as well (e.g. Dahal et al. 2023). Accordingly, one can roughly estimate the quality of rockfalls prediction by the deviation of Ω from the percentage $\Omega = 100\%$, which corresponds to random prediction results. Low values of Ω characterize accurate predictions, while as Ω increases toward 100% the quality of results decreases. Graphically in the errors diagram, the diagonal line from the upper left corner to the lower right corner corresponds to the points for which it holds $\Omega = \eta + \alpha = 100\%$, namely to the results that can be obtained by random guess. The more the results are distant from the diagonal line (corresponding to a random guess) and close to the origin of the axes (i.e., for low fraction of both alarms and failures), the better the forecast performance.

The forecasting scores, obtained for the four different scenarios and for the selected PGA thresholds, considering the landslide points reported by Govi (1977), are shown in Fig. 3 and listed in Table 2. The forecasting results, obtained only from the spatial distribution of slope angles and with no information about ground shaking, are provided for comparison.

The landslide inventory prepared by Govi (1977) after the seismic sequence includes 272 polygons, corresponding to a subset of the 1007 landslide points, consisting almost entirely by rockfalls. The polygons have area in the range 389 m^2–72,753 m^2. We used this subset of the inventory to measure the performance of rockfall modeling, counting the number of simulated trajectories crossing each landslide body.

Physically based rockfall assessment was performed using the TINITALY digital elevation model, with a 10 m grid cell size (Tarquini et al. 2007), and terrain parameters entering the STONE model were extracted using the 1:100,000 lithological map of Italy by Bucci et al. (2022). The high resolution of elevation data dictates the resolution of the simulated rockfall trajectories. This implies that using point landslide data to assess results would be difficult at this level of detail, thus we opted for the polygonal set of the inventory, in the following.

Figure 4 shows histograms of the distribution of the number of polygonal landslides (a, b; yellow bars) and the total

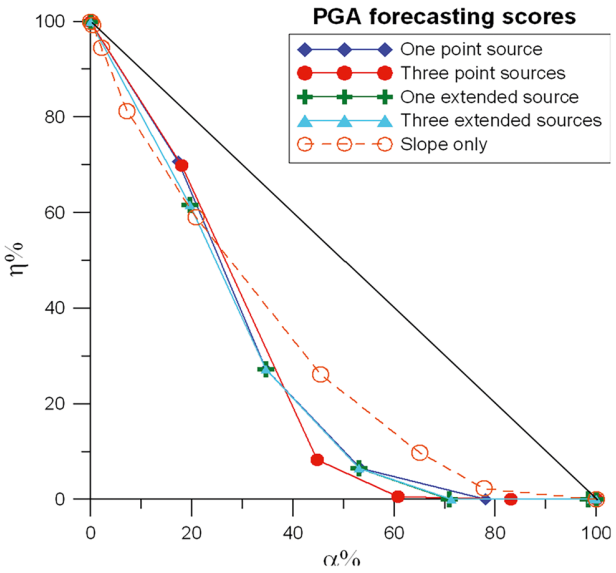

Fig. 3 Errors diagram for the predictive analysis of rockfalls versus modeled ground shaking (PGA [gal]).The percentage of failures to predict is η%, and α% is the percentage of total area selected by a specific PGA threshold. The diagonal line corresponds to the results of a random guess ($\eta + \alpha = 100\%$). The different curves correspond to the results obtained for the four different models and the PGA thresholds listed in Table 2. The prediction results, obtained based only on the spatial distribution of ground slope angles are provided for comparison

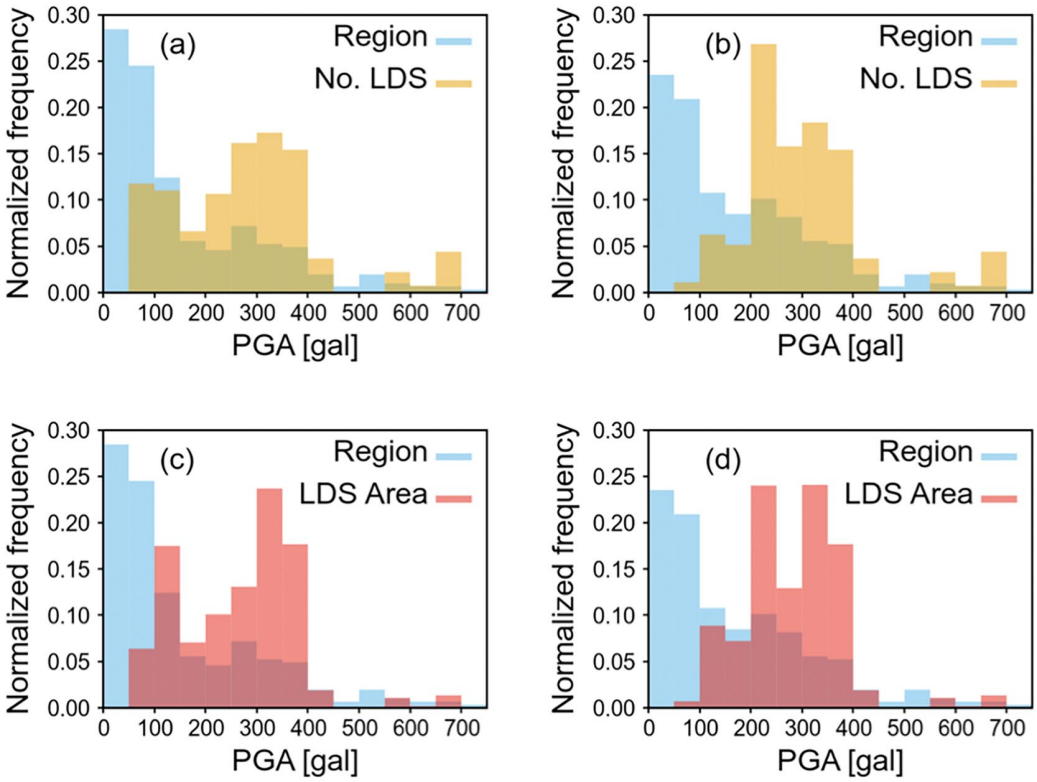

Fig. 4 Distribution of the number of observed landslides (LDS; **a, b**) and of total landslide area (**c, d**) as a function of PGA values, in intervals of 50 gal. In all of the plots, the background blue distribution of the number of PGA grid cells (*cf.* Fig. 1, top row). The distributions in (**a**) and (**c**) correspond to one point source, in (**b**) and (**d**) to three point sources

landslide area (c, d; red bars) as a function of PGA, for the approximations of one and three point sources, respectively, corresponding to panels (a) and (b) in Fig. 2. All of the distributions compare the number/area histograms to the overall distribution of PGA in the study area (blue bars). One can see that simulating three point sources gives an advantage with respect to the case based on one source only, both in terms of number of landslides associated with larger values of PGA, and in terms of the area occupied by the corresponding polygons. This can be considered as a quantitative evidence of the conclusions drawn from visual assessment of the results in Figs. 2 and 3. This analysis compares with that of Dahal et al. (2023).

Eventually, Fig. 5 shows the actual simulations of rockfall trajectories with the three-dimensional model STONE. The four different maps distinguish different approximations both on the modeled earthquake scenarios side and on the rockfall modeling side. Specifically, two different scenarios are considered for the earthquake sources (one point source—left panels, and three point sources—right panels) and two different parametrizations are used for the coupling between shake maps and rockfall initiation points (linear rescaling of PGA—top panels, and non-linear rescaling—bottom panels, see Alvioli et al. (2024) for details on the functional forms).

Visual assessment of the results clearly suggests that the three-source description has an advantage with respect to the one-source case. That could be expected, considering the ground shaking maps alone (Fig. 2a, b), which already suggest better agreement on the three-source case. On the other hand, the approximations for the PGA-rockfall sources coupling seem equally valid, and it is difficult to understand the balance of positive and negative predicted areas with respect to observed landslides. Thus, in Table 3 we reported numerical values describing the agreement between the output of the model STONE and observed landslides. The model calculates rockfall trajectories, and the output is a raster containing the count of the number of trajectories crossing each grid cell.

The table shows the percentage area of rockfall polygons crossed by at least one simulated trajectory, in the four dif-

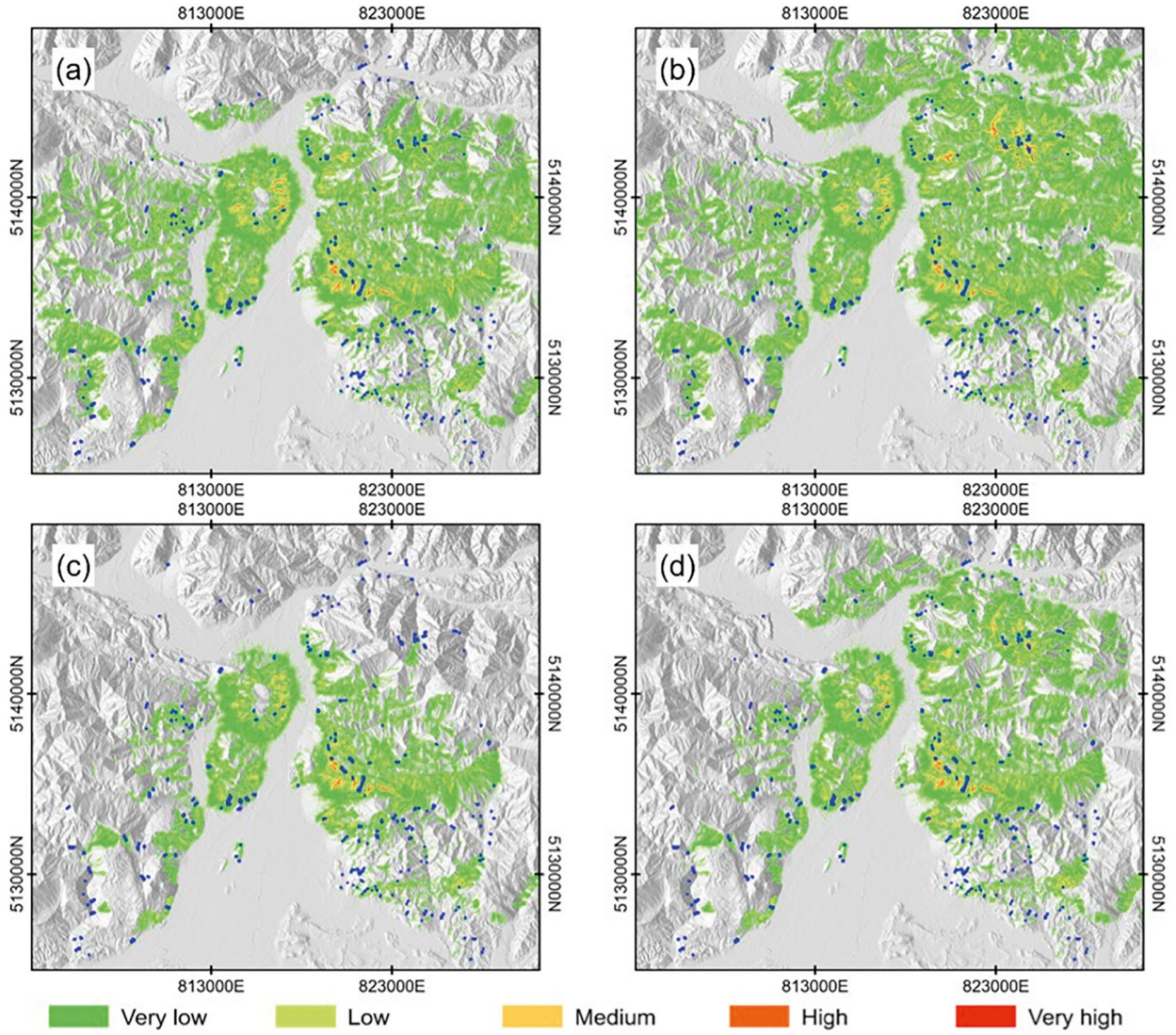

Fig. 5 Maps of cumulative counts of trajectory obtained with STONE. We adopted two different approximations for the seismological simulations (left panels: one point source; right panels: three point sources), and two different approximations for the selection of dynamic rockfall sources from the static rockfall sources (top panels: linear rescaling of PGA; bottom panels: non-linear rescaling of PGA using a normalized tunable sigmoid function, see Alvioli et al. 2023). Blue polygons represent observed rockfalls. The trajectory counts are classified with a head/tail algorithm. See Table 3 for numerical results

Table 3 Agreement between probabilistic, modeled rockfall run out and observed rockfall polygons. The first two rows represent the percentage of rockfall area intersected by at least one rockfall trajectory; the last row represent the percentage gain using the PGA map obtained from three point sources, with respect to using the one corresponding to one point source

	Linear	NTSF 1
One point source	68.5%	52.5%
Three point sources	71.4%	61.3%
Gain	4.2%	16.3%

ferent cases, and the percentage gain using the PGA obtained from three seismic sources with respect to a single source, in both PGA-rockfall initiating points coupling schemes. The gain is larger in the non-linear coupling case, 16.3% *vs.*4.2% for the linear case. That is at the expense of overall lower percentage area correctly predicted as unstable in both one-source and three-sources earthquake simulations.

3 Discussion and Conclusions

The aim of this study is to analyze the spatial distribution pattern of rockfalls triggered by the FVG 1976 seismic sequence, considering various earthquake scenarios. We utilized a physics-based approach to compute the corresponding PGA and landslides density at a regular grid of 2 × 2 km, incorporating both point and extended source models for one earthquake (the main shock), as well as an aggregated scenario of three earthquakes (main shock and the strongest aftershocks with Mw close to 6.0) shown in Table 1 and Fig. 1. Next, we compared the spatial distribution patterns of landslides/rockfalls and PGAs for the site of interest using the Quantum Geographic Information System (QGIS) tool. Overlaying both datasets in a geographic information system enabled us to assess whether ground motion simulation scenarios accurately capture the observed distribution patterns of landslides. Additionally, we investigated which earthquake scenario, if any, effectively captures this pattern.

Associating the spatial distribution pattern of observed landslides, triggered by the Friuli 1976 seismic sequence, with the PGA pattern computed for the main shock using a point source model seems unsatisfactory, as compared to those obtained for the aggregated scenario of the seismic sequence (Fig. 2a, b). Additionally, we tested the extended source model for both the main shock and the three earthquakes aggregated scenario. Though the resulting ground motion simulations slightly improved the spatial pattern, compared to those from the single point source model, the improvement was not as evident as that achieved with the three point sources model (see Fig. 2).

The map depicting the difference between the PGA maps of the three earthquakes aggregated scenario and the main shock (both from point source models), combined with rockfall density, supports this conclusion (Fig. 6). The map shows that the aftershocks of the Mw 6.5 1976 Friuli earthquake significantly influenced the PGA ground shaking pattern, prevailing in the north-eastern parts of the study area, where high rockfall density is observed as well. This conclusion is corroborated by the error diagram analysis, shown in Fig. 3, which shows how well the modeled ground shaking "predicts" the spatial distribution of rockfalls, comparing the percentage of failures η and the percentage of area α selected by a specific PGA threshold, for increasing threshold values. The curves obtained for the four different models and the PGA thresholds listed in Table 2, show that the three point source scenario best capture the spatial pattern of observed landslides. Moreover, all modeled ground shaking scenarios display better prediction results than those obtained considering only the spatial distribution of ground slope angles, which are provided for comparison.

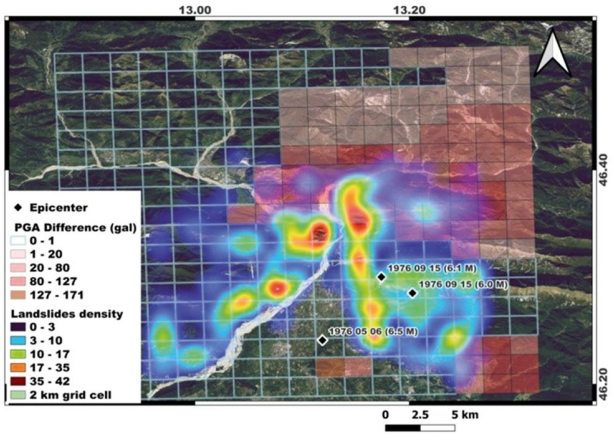

Fig. 6 Map of the difference between PGA computed for three earthquake aggregated scenario and one main earthquake for point source model compared with the density of observed landslides

The complete modeling chain considers physical three-dimensional modeling of rockfall trajectories, coupled with ground-shaking scenarios. High resolution analysis gives the opportunity of considering the polygonal subset of the inventory compiled after the FVG 1976 seismic sequence. We analyzed the distribution of number of landslides and landslide area as a function of PGA from the two-point source scenarios, with the same conclusions of the 2 × 2 km grid analysis (Fig. 4). Moreover, runs of the code STONE for a probabilistic assessment of rockfall trajectories in the two scenarios with point sources at 10 m resolution, suggests a better match with observed landslide polygons and the scenario with three point sources (Fig. 5, Table 3). This study suggests us further exploring the numerous possibilities offered by the combined use of physics-based methods, for both earthquake and rockfall modeling, and their possible contribution towards a better understanding of the triggering mechanisms of Coseismic rockfalls, including the influence of topography on seismic ground shaking.

The results of the current study highlighted an important aspect: the potential of the strongest aftershocks of the 1976 FVG seismic sequence on the final spatial distribution pattern of these rockfalls cannot be overlooked. It is crucial to consider that the susceptibility to landslides might increase in the aftermath of the main shock. In fact, the shaking caused by earthquake can destabilize slopes by loosening the soil or rock material. This increased instability can lead to landslides occurring both during and after the shaking. Moreover, aftershocks can continue to shake the ground and further weaken already compromised slopes, potentially triggering new landslides/rockfalls.

The spatial distribution pattern and density of coseismic landslides induced by the 1976 Friuli sequence well corresponds to the peak ground acceleration obtained modeling the main shock along with the two strongest aftershocks. This is quite evident in the maps showing the difference between the PGA estimated separately for the main shock and the sequence. It is apparent that the PGA values from the sequence display a better correlation with the coseismic landslide density map, compared to those from the main shock alone.

Acknowledgments The authors are grateful to Hany M. Hassan for the insightful discussions and for his contribution to manuscript preparation. The authors are also indebted to Giuliano Panza, Fabio Romanelli, Andrea Magrin and the team who developed the NDSHA modeling package, some modules of which were used in this study. The study is a contribution to the RETURN Extended Partnership (European Union Next-Generation EU—National Recovery and Resilience Plan—NRRP, Mission 4, Component 2, Investment 1.3 –D.D. 1243 2/8/2022, PE0000005).

References

Aki K (1987) Strong motion seismology. In: Erik M, Toksöz M (eds) Strong ground motion seismology, NATO ASI series, series C: mathematical and physical sciences, vol 204. D. Reidel Publishing Company, Dordrecht, pp 3–39. https://doi.org/10.1007/978-94-017-3095-2_1

Akkar S, Bommer JJ (2007) Prediction of elastic displacement response spectra in Europe and the Middle East. Earthq Eng Struct Dyn 36(10):1275–1301. https://doi.org/10.1002/eqe.679

Alvioli M, Guzzetti F, Marchesini I (2020) Parameter-free delineation of slope units and terrain subdivision of Italy. Geomorphology 358:107124. https://doi.org/10.1016/j.geomorph.2020.107124

Alvioli M, Santangelo M, Fiorucci F, Cardinali M, Marchesini I, Reichenbach P, Rossi M, Guzzetti F, Peruccacci S (2021) Rockfall susceptibility and network-ranked susceptibility along the Italian railway. Eng Geol 293:106301. https://doi.org/10.1016/j.enggeo.2021.106301

Alvioli M, De Matteo A, Castaldo R, Tizzani P, Reichenbach P (2022) Three-dimensional simulations of rockfalls in Ischia, southern Italy, and preliminary susceptibility zonation. Geomat Nat Haz Risk 13(1):2712–2736. https://doi.org/10.1080/19475705.2022.2131472

Alvioli M, Falcone G, Mendicelli A, Mori F, Fiorucci F, Ardizzone F, Moscatelli M (2023) Seismically induced rockfall hazard from a physically based model and ground motion scenarios in Italy. Geomorphology 429:108652. https://doi.org/10.1016/j.geomorph.2023.108652

Alvioli M, Poggi V, Peresan A, Scaini C, Tamaro A, Guzzetti F (2024) A scenario-based approach for immediate post-earthquake rockfall impact assessment. Landslides 21:1–16. https://doi.org/10.1007/s10346-023-02127-2

Aoudia A, Saraò A, Bukchin B, Suhadolc P (2000) The 1976 Friuli (NE Italy) thrust faulting earthquake: a reappraisal 23 years later. Geophys Res Lett 27(4):573–576. https://doi.org/10.1029/1999GL011071

Bressan G, Barnaba C, Bragato P, Ponton M, Restivo A (2018) Revised seismotectonic model of NE Italy and W Slovenia based on focal mechanism inversion. J Seismol 22:1563–1578. https://doi.org/10.1007/s10950-018-9785-2

Bucci F, Santangelo M, Fongo L, Alvioli M, Cardinali M, Melelli L, Marchesini I (2022) A new digital lithological map of Italy at 1:100,000 scale for geo-mechanical modeling. Earth Syst Sci Data 14:4129–4151. https://doi.org/10.5194/essd-14-4129-2022

Cancani A (1904) Sur l'emploi d'une double échelle sismique des intensités, empirique et absolue. Gerl Beitrage Geophys 2:281e283

Dahal A, Alejandro Castro-Cruz D, Tanyaş H, Fadel I, Mai PM, van der Meijde M, van Westen C, Huser R, Lombardo L (2023) From ground motion simulations to landslide occurrence prediction. Geomorphology 441:108898. https://doi.org/10.1016/j.geomorph.2023.108898

DISS, Working Group (2021) Database of Individual Seismogenic Sources (DISS), Version 3.3.0: a compilation of potential sources for earthquakes larger than M 5.5 in Italy and surrounding areas. Istituto Nazionale di Geofisica e Vulcanologia (INGV). https://doi.org/10.13127/diss3.3.0

Fan X, Scaringi G, Korup O, West AJ, van Westen CJ, Tanyas H, Hovius N, Hales TC, Jibson RW, Allstadt KE (2019) Earthquake-induced chains of geologic hazards: patterns, mechanisms, and impacts. Rev Geophys 57(2):421–503. https://doi.org/10.1029/2018RG000626

Gorshkov AI, Panza GF, Soloviev AA, Aoudia A, Peresan A (2009) Delineation of the geometry of nodes in the Alps-Dinarides hinge zone and recognition of seismogenic nodes ($M \geq 6$). Terra Nova 21(4):257–264. https://doi.org/10.1111/j.1365-3121.2009.00879.x

Govi M (1977) Photo-interpretation and mapping of the landslides triggered by the Friuli earthquake (1976). Bull Eng Geol Environ 15(1):67–72. https://doi.org/10.1007/BF02592650

Gusev AA (1983) Descriptive statistical model of earthquake source radiation and its application to an estimation of short period strong motion. Geophys J R Astron Soc 74:787–800. https://doi.org/10.1111/j.1365-246X.1983.tb01904.x

Gusev AA (2011) Broadband kinematic stochastic simulation of an earthquake source: a refined procedure for application in seismic hazard studies. Pure ApplGeophys 168(1–2):155–200. https://doi.org/10.1007/s00024-010-0156-3

Guzzetti F, Crosta G, Detti R, Agliardi F (2002) STONE: a computer program for the three-dimensional simulation of rockfalls. Comput Geosci 28:1079–1093. https://doi.org/10.1016/S0098-3004(02)00025-0

Igel H (2016) Computational seismology: a practical introduction. https://doi.org/10.1093/acprof:oso/9780198717409.001.0001

Jibson RW (2011) Methods for assessing the stability of slopes during earthquakes—a retrospective. Eng Geol 122(1–2):43–50. https://doi.org/10.1016/j.enggeo.2010.09.017

Keefer DK (2000) Statistical analysis of an earthquake-induced landslide distribution—the 1989 Loma Prieta, California event. Eng Geol 58(3–4):231–249. https://doi.org/10.1016/S0013-7952(00)00037-5

Luzi L, Pergalani F (2000) A correlation between slope failures and accelerometric parameters: the 26 September 1997 earthquake (Umbria–Marche, Italy). Soil Dyn Earthq Eng 20(5–8):301–313. https://doi.org/10.1016/S0267-7261(00)00063-4

Molchan GM (1990) Strategies in strong earthquake prediction. Phys Earth Planet Inter 61(1–2):84–98

Molchan GM (1997) Earthquake prediction as a decision-making problem. Pure Appl Geophys 149:233–247. https://doi.org/10.1007/BF00945169

Panza GF, Vaccari F, Cazzaro R (1997) Correlation between macroseismic intensities and seismic ground motion parameters. Ann Geophys 15:1371e1382

Panza GF, Romanelli F, Vaccari F (2001) Seismic wave propagation in laterally heterogeneus anelastic media: theory and applications to seismic zonation. Adv Geophys 43:1–95. https://doi.org/10.1016/S0065-2687(01)80002-9

Panza GF, La Mura C, Peresan A, Romanelli F, Vaccari F (2012) Seismic hazard scenarios as preventive tools for a disaster resil-

ient society. Adv Geophys 53:93–165. https://doi.org/10.1016/B978-0-12-380938-4.00003-3

Pavlov VM (2009) Matrix impedance in the problem of the calculation of synthetic seismograms for a layered-homogeneous isotropic elastic medium. Izv Phys Solid Earth 45:850–860. https://doi.org/10.1134/S1069351309100036

Peresan A, Gentili S (2018) Seismic clusters analysis in northeastern Italy by the nearest-neighbor approach. Phys Earth Planet Inter 274:87–104. https://doi.org/10.1016/j.pepi.2017.11.007

Rovida A, Locati M, Camassi R, Lolli B, Gasperini P, Antonucci A (2022) Catalogo Parametrico dei Terremoti Italiani (CPTI15), versione 4.0 [Data set]. Istituto Nazionale di Geofisica e Vulcanologia (INGV). https://doi.org/10.13127/cpti/cpti15.4

Slejko D, Neri G, Orozova I, Renner G, Wyss M (1999) Stress field in Friuli (NE Italy) from fault plane solutions of activity following the 1976 main shock, Bull. Seism Soc Am 89:1037–1052

Tanyaş H, van Westen CJ, Persello C, Alvioli M (2019) Rapid prediction of the magnitude scale of landslide events triggered by an earthquake. Landslides 16:661–676. https://doi.org/10.1007/s10346-019-01136-4

Tarquini S, Isola I, Favalli M et al (2007) TINITALY/01: a new triangular irregular network of Italy. Ann Geophys 50:407–425. https://doi.org/10.4401/ag-4424

Tiwari B, Ajmera B, Dhital S (2017) Characteristics of moderate-to large-scale landslides triggered by the M w 7.8 2015 Gorkha earthquake and its aftershocks. Landslides 14:1297–1318. https://doi.org/10.1007/s10346-016-0789-0

Valagussa A, Frattini P, Crosta GB (2014) Earthquake-induced rockfall hazard zoning. Eng Geol 182:213–225. Special issue on: the long-term geologic hazards in areas struck by large-magnitude earthquakes. https://doi.org/10.1016/j.enggeo.2014.07.009

Worden CB, Thompson EM, Hearne M et al (2020) Shake map manual online: technical manual, user's guide, and software guide. Geological Survey, US. https://doi.org/10.5066/F7D21VPQ